Title
(Photo)Electrocatalytic CO2 Reduction at the Defective Anatase TiO2 (101) Surface

Journal
ACS Catalysis, 10(7)

ISSN
2155-5435

Authors
Liu, Ji-Yuan
Gong, Xue-Qing
Li, Ruoxi
et al.

Publication Date
2020-04-03

DOI
10.1021/acscatal.0c00947

Peer reviewed

(Photo)electrocatalytic CO_2 reduction at the defective anatase TiO_2 (101) surface

Ji-Yuan Liu[1,2], Xue-Qing Gong[2] Ruoxi Li,[3] Haotian Shi,[4] Stephen B. Cronin,[3,4] Anastassia N. Alexandrova[1,5,*]

[1]*Department of Chemistry and Biochemistry, University of California, Los Angeles, Los Angeles, CA, 90095, USA*

[2]*Key Laboratory for Advanced Materials, Center for Computational Chemistry and Research Institute of Industrial Catalysis, School of Chemistry and Molecular Engineering, East China University of Science and Technology, 130 Meilong Road, Shanghai 200237, P. R. China.*

[3]*Department of Electrical and Computer Engineering, and* [4]*Department of Chemistry, University of Southern California, Los Angeles, California 90089, USA*

[5]*California NanoSystems Institute, Los Angeles, CA, 90095, USA*

Corresponding Author e-mail: ana@chem.ucla.edu

ABSTRACT:

Excessive carbon dioxide (CO_2) emissions by combustions of fossil fuels is linked to the global warming and rapid climate change. One promising route to lowering the concentration of CO_2 in the atmosphere is to reduce it to useful small molecules via photoelectrocatalytic hydrogenation, which would enable solar energy storage with a zero carbon emission cycle and perform a more efficient separation of the photogenerated electron and hole pair than pure photocatalysis. Indeed, photoelectrocatalytic CO_2 reduction has been an intense focus of research. Using density functional theory (DFT), we studied CO_2 reduction reaction on the defective anatase TiO_2 (101) surface, at both the solvent/catalyst and the electrolyte/catalyst interfaces. The analysis of the electronic structure of the surface shows a contrast between the solvent/catalyst and the electrolyte/catalyst interfaces, which results in the two corresponding catalytic cycles being distinct. Our study explains at the electronic and mechanistic level why methanol is the main product in the presence of the electrolyte and the overpotential not only controlled by reaction process but also the diffusion process.

Introduction

The concentration of carbon dioxide (CO_2) in the atmosphere, one of the major greenhouse gases, grew by more than 6% in the past decades, causing rapid climate change[1]. Thus, the conversion of CO_2 is an urgent challenge, which attracts plenty of attention in research. Many efforts have been made to reduce this inert molecule to useful chemicals such as carbon monoxide, formic acid, and fuel molecules such as methane and methanol[2–5]. The most common methods are electrocatalysis and photocatalysis, of which the latter is particularly attractive since it utilizes solar energy to achieve the zero-carbon emission reduction process. However, the energy efficiency of photocatalysis is very low (only 3.8% of that of electrolysis)[6]. In this vein, photoelectrocatalysis is on the rise in this field, because it inherits the advantages of photocatalysis (the use of solar energy), and at the same time avoids the disadvantages such as low photogenerated electron-hole separation efficiency, re-oxidation of the products, and the insufficient conduction band edge level[7].

Halmann reported a pioneering work on photoelectrocatalytic reduction of CO_2 on an irradiated p-type

semiconductor, GaP, in the presence of an applied bias potential[8]. Barton et al. reached a nearly 100% faradaic efficiency of CO_2 photoelectrochemical reduction at p-GaP electrodes with homogenous pyridinium ion catalyst[9]. Recently, Qiu et al. achieved artificial photosynthesis by using TiO_2-passivated InP nanopillar photocathodes under illumination[10]. Song et al. developed a highly selective and efficient photoelectrodes by photolithographically plating a nanoporous Au film on Si electrode[11]. CO, HCOOH and CH_3OH are the main products of the photoelectroreduction in these experimental works.

On the theoretical side, many methods have been recently implemented to apply electrochemical potential in quantum chemical calculation under the periodic boundary conditions[12,13], including charging the slab and providing a compensating homogenous background charge[14–16], explicit ions[17,18], the grand canonical potential kinetics[19] and the linear free energy relationship for the electrochemical potential with the computational hydrogen electrode (CHE) model[20], where some of them have been already applied on the semiconductor system. The solvent/electrolyte, which plays an important role in the electrochemical process[21], is most of the time treated implicitly. However, all applications of these methods involve the electrochemical CO_2 reduction reaction (CO_2RR) on a metallic cathode. Simulations have not yet addressed the (photo)electrocatalytic CO_2RR on semiconductor cathodes, and it is still unknown how the applied electrochemical potential and solvent affect the heterogeneous CO_2RR at such interfaces of semiconductors.

The cathode in a (photo)electrochemical cell can directly convert CO_2 through a series of multi-electron hydrogenation processes:

$$CO_2 + 2H^+ + 2e^- = HCOOH \quad (1)$$

$$CO_2 + 2H^+ + 2e^- = CO + H_2O \quad (2)$$

$$CO_2 + 4H^+ + 4e^- = HCHO + H_2O \quad (3)$$

$$CO_2 + 6H^+ + 6e^- = CH_3OH + H_2O \quad (4)$$

$$CO_2 + 8H^+ + 8e^- = CH_4 + 2H_2O \quad (5),$$

to generate useful species, or indirectly further hydrogenate the intermediates:

$$CO + 2H^+ + 2e^- = HCHO \quad (6)$$

$$HCHO + 2H^+ + 2e^- = CH_3OH \quad (7)$$

$$HCHO + 4H^+ + 4e^- = CH_4 + H_2O \quad (8),$$

while the oxygen evolution reaction should occur on the anode, giving rise to protons which can migrate to the cathode. The TiO_2 film is a common material that would be deposited on a metallic electrode in the electrochemical cell, or the semiconductor electrode in photoelectrochemical cell, because of its stability against corrosion, high current efficiency, and low valence band edge to fulfill a current cycle[22–28]. For instance, the InP photocathode gets significant degraded after 0.5 h illumination under the photoelectrochemical condition, whereas the TiO_2-passivate one keeps stable for at least 12 h[10]. Therefore, the TiO_2 material in this circumstance plays an important role as a catalyst and a protector rather than a light harvester. Understanding the mechanism of (photo)electrocatalytic CO_2RR requires consideration of the TiO_2 surface is in the electrochemical condition. Moreover, the overpotential is a key factor to understand the (photo)electroreaction as well, which was theoretically thought controlled by binding energies in each elementary step[20]. Recently, we elucidated a part of the mechanism of photoreduction of CO_2 on the defective anatase TiO_2 (101) surface, based on density functional theory (DFT) calculations[29]. This study revealed the essential role of the oxygen vacancy in the CO_2RR process. In this work, we consider CO_2RR on defective anatase TiO_2 (101) under an electrochemical potential, to simulate the (photo)electrocatalytic scenario and to elucidate the difference in the adsorption and reaction processes on

the pristine and defective surfaces, and at the vacuum/catalyst (V/C), solvent/catalyst (S/C) and electrolyte/catalyst (E/C) interfaces.

Computational Details

Spin-polarized density functional theory (DFT) calculations corrected by on-site Coulomb interaction was performed with the Vienna Ab initio Simulation Package (VASP)[30–33]. The projected augment-wave[34,35] and the Perdew, Burke and Ernzerhof (PBE) generalized gradient approximant functional[36,37] were utilized throughout this study. A cutoff energy of 400 eV was set, and a 3.5 eV effective U value was applied to the 3d orbitals of Ti to better describe the electron localization at the oxygen vacancy. The 0.5 M KCl aqueous solution with the dielectric constant of 78.4 was treated implicitly, using the VASPsol[38,39] code, in the S/C and E/C interface simulations. All the transition state configurations were located by climbing image nudged elastic band (CI-NEB) method[40]. The Bader charge analysis[41] was utilized to study the charge distributions.

The anatase TiO_2 (101) was modeled as a symmetric slab, built from a (3×1) supercell of an optimized anatase cell. It consisted of 30 atomic layers with the middle six layers fixed, as illustrated in Figure 1. In this model, the surface slab consisted of the surface area (the 1st, 3rd , 28th and 30th atomic layers), the subsurface area (the 2nd, 4th~6th , 25th~27th and 29th atomic layers), the transition area (the 7th~12th and 19th~24th atomic layers), and the bulk area (the 13th~18th atomic layers), of which the last two were called the interlayer area in this work. A 20 Å vacuum layer was placed between the slabs to avoid their interactions along z-direction. The surface oxygen atoms in the center of the outermost oxygen layers of both sides of the slab were removed to simulate the defective surface. Reactant molecules were symmetrically put on both sides to counter the possible polarization of dipole.

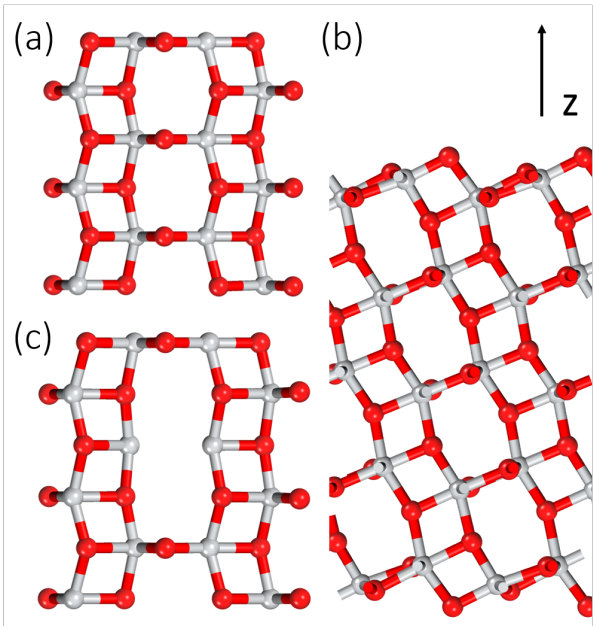

Figure 1. The top (a) and side (b) views of the pristine surface, and the top (c) view of the defective surface anatase. The silver and red spheres are the Ti and O atoms, respectively.

The applied electrochemical potential was simulated by the linearized Poisson-Boltzmann equation method[42] described by the VASPsol code. In this method, a certain net charge q is introduced into the electrode slab and the corresponding compensating background charge $q_{bg} = -q$ is added into the electrolyte, in order to keep the whole system charge-neutral. The absolute electrode potential, ϕ, is obtained by subtracting the Fermi energy from the energy level of electrolyte, and the result numerically equals the work function. Therefore, the applied electrochemical potential versus standard hydrogen electrode, ϕ_{SHE}, is given by

$$\phi_{SHE} = \phi - 4.44 \quad (9),$$

where 4.44 V is the recommended absolute potential of the H^+/H redox pair in aqueous solutions[43]. Due to the existence of net charge, the total DFT energy should be grand canonically corrected as the electronic free energy[44], E^{free}:

$$E^{free} = E_{DFT}(q) + q\phi \quad (10),$$

where E_{DFT} is the calculated total energy of the corresponding net charge. The extrapolating linear, and quadratic fittings were applied for the relationships between q and ϕ_{SHE}, and E^{free} and ϕ_{SHE}, respectively, with both coefficients of determination being over 0.999.

Benefited from this model, we can retrieve the adsorption, reaction and activation energies during the DFT calculation. The adsorption energy for each molecule, E_{ads}, was calculated by

$$E_{ads} = \frac{1}{2}\left(E^{free}_{adsorbate@slab} - 2E_{adsorbate} - E^{free}_{slab}\right) \quad (11),$$

where $E^{free}_{adsorbate@slab}$ and E^{free}_{slab} stand for the calculated electronic free energies of the cathode slab with and without adsorbates, respectively, and $E_{adsorbate}$ represents the calculated energy of the corresponding adsorbate.

Only hydrogenation half reaction was considered in the current work. The protons consumed in the photo-reduction and cathode half reactions were supposed generated from the corresponding photo-oxidation and anode half reactions. In each single electronic hydrogenation half reaction, a proton and an electron which are spontaneously produced by introduced hydrogen[45,46] atom would participate step in the photo- and (photo)electrochemical reaction. To avoid misunderstanding, the formaldehyde, HCHO, is denoted as CH_2O.

Results and discussion

Charge distribution in the pristine anatase TiO_2 (101) surface slab in various conditions

The electronic properties of species in the surface area at the anatase surface, including their deviations from those in the bulk anatase and variations in the presence of the solvent, were analyzed in the beginning. The anatase TiO_2 bulk consists of saturated 6-coordinated Ti and 4-coordinated O atoms, whereas at the V/C interface there are exposed 5-coordinated Ti and 2-coordinated O atoms. The unsaturated 2-coordinated O species at the surface are the bridging oxygens. Due to the undercoordination, these atoms lack 0.12 e compared to the average number of electrons, $\overline{q}$, on the O ones in the bulk (black line, Figure 2b). Hence, these bridging oxygen atoms have a greater capacity to accept electrons, *i.e.* act as oxidants. Naturally, the opposite is true for the unsaturated Ti atoms at the surface, of which $\overline{q}$ have 0.03 e greater than those of the bulk Ti atoms (black line, Figure 2c). Therefore, interfacial Ti atoms are more reducing than bulk Ti ones, and that benefits the adsorptions of oxidants at the V/C interface. There are also some fluctuations on the $\overline{q}$ in the subsurface area. Note as well that $\overline{q}$ is

symmetric for the two sides of the slab, indicating the perfectly countered dipole polarization.

The implicit aqueous solvent is introduced at the interface next, and the relationship between the potential and z values as well as the electric double layer can be confirmed in the Figure S1. The $\overline{q}$ in the surface area becomes much closer to that in the bulk (red lines in Figure 2b and 2c). Compared with the V/C interface, the bridging O atoms at the S/C interface lose fewer electrons, and the Ti atoms gain fewer electrons, *i.e.* the surface sites at the S/C interface are slightly passivated as compared to those at the V/C interface. This is a result of the re-polarization of the slab caused by the electrostatic interaction with the polar aqueous solvent. While at the E/C interface, the $\overline{q}$ in the surface area increases, compared with the one at the S/C interface, which is consistent with the charge distribution of working semiconductor cathode (see green, yellow and blue lines in the Figure 2b and 2c). This increment leads to an enhancement on the reducing performance of the interfacial Ti and a degeneration on the oxidizing performance of the bridging oxygens. Therefore, only adsorption of polar oxidants at the interface should be improved in the electrolyte, compared to the interface with the aqueous solvent. The inner layers in the slab experience little shifts in $\overline{q}$, due to shielding from the solvent and smaller geometric relaxation than at the interface. Figure S2 further illustrates the charge density difference between the charged and solvated systems. The introduced charge concentrates at the surface, and in particular on the surface oxygen atoms, whereas the inner-layer $\overline{q}$ changes relatively little with the slab charging.

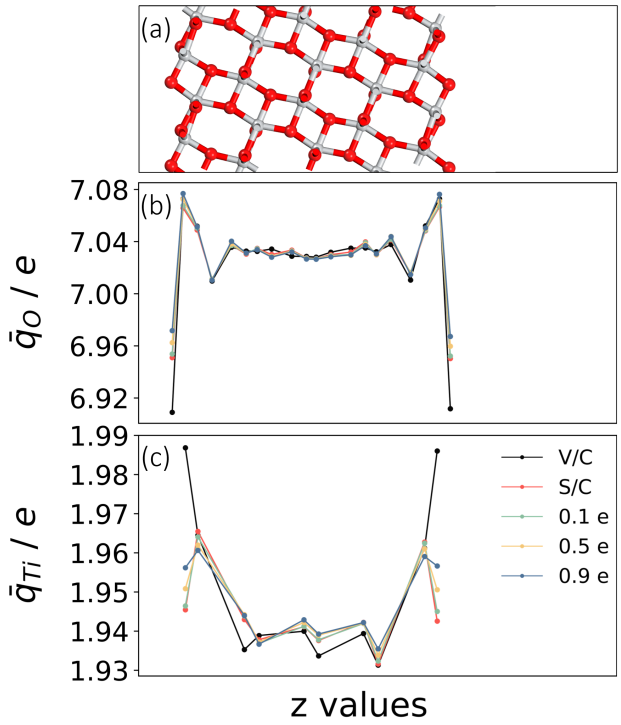

Figure 2. The Bader charge analysis on average (per atom) electronic quantity, $\overline{q}$, of each atomic layer in the pristine surface slab as a function of z, at the V/C and S/C interfaces: (a) is the side view of the pristine surface slab; (b) and (c) the $\overline{q}$ of each oxygen and titanium atomic layer, respectively. 0.1 e, 0.5 e, 0.9 e stand for the net extra charge of introduced into the charged systems. (a), (b) and (c) share the same x-axis.

The adsorption and reaction processes at the solvent/catalyst (S/C) interface of the defective surface

The adsorption energies of all involved reactants and products, on both the pristine and the defective surfaces as the V/C and S/C interfaces were calculated. In agreement with the above charge analysis, the solvent effect electronically passivates the surface sites and weakens all the adsorption processes with different degrees (see Table 1), which has a similar trend as the study with various explicit solvent[47]. CO_2 species, the main reactant, is no longer adsorbed on either surface, despite the positive effect of the oxygen vacancy (O_v) sites on the adsorption, which is consistent with the early computational work on TiO_2 cluster model[48]. CO is bound to both surfaces with a rather small adsorption energy, and thus remains the carbon source for the reduction reaction. Other carbon-based species, e.g. carbonate, could be present and participate in the entire reduction process not considered in this work. As for the products, the desorption become much easier from the S/C interface than from the V/C interface. At the pristine surface, the adsorption energies of CH_2O and CH_3OH are halved with the presence of the aqueous solvent, suggesting the direct desorption of these species in mild conditions. On the other hand, at the defective surface, these species appear to be trapped at the O_v site, with adsorption energies below -0.63 eV, despite the electronic passivation. Because of the strong adsorption of CH_2O, it could undergo further reduction. CH_3OH can bind to the surface endothermically by 0.19 eV, and be released without an energy barrier. CH_4, which has adsorption energies compatible with its release as a product, is hardly influenced by the solvent effect, as expected based on its insignificant polarity.

Table 1. The adsorption energies for reactant and product molecules on both pristine and defective surfaces. The corresponding configurations can be found in Figure S3.

	Adsorption Energy / eV			
	Pristine surface		Defective surface	
Adsorbate	V/C	S/C	V/C	S/C
CO_2	-0.07	0.18	-0.38	0.11
CO	-0.40	-0.15	-0.71	-0.20
CH_2O	-0.72	-0.36	-1.49	-0.90
CH_3OH	-0.89	-0.44	-1.21	-0.63
CH_4	-0.02	0.01	-0.10	0.35

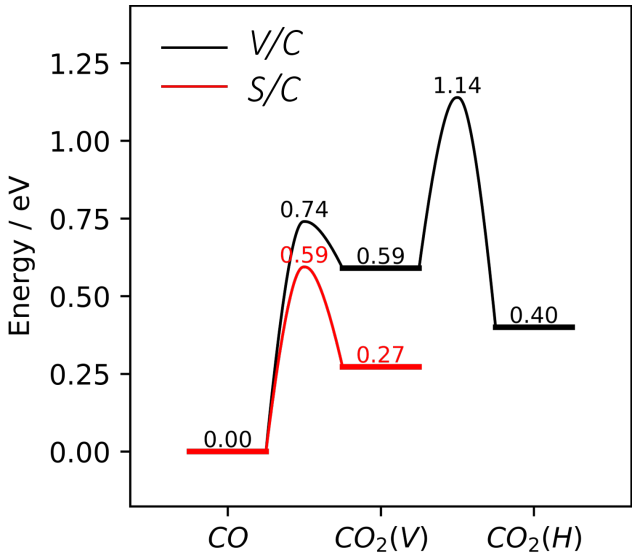

Figure 3. The calculated reaction profile of the conversion between CO_2 and CO. The x-axis stands for the reaction coordinate. All corresponding configurations are displayed in Figure S4.

The conversion between CO_2 and CO species at both V/C and S/C interfaces of the defective surface were calculated and illustrated in Figure 3 and S3. At the V/C interface, the main carbon source, CO_2, preferentially occupies the O_v site, initially assuming a "horizontal" configuration, CO_2(H) (see Figure S4). It can transform to a "vertical' configuration, CO_2(V), with an activation energy of 0.74 eV and endothermicity of 0.19 eV. The CO_2(V) intermediate can exothermically produce CO and simultaneously cure the O_v site, forming the pristine surface (the corresponding barrier is 0.15 eV). Since CO_2 cannot bind to the defective surface at the S/C interface, only the oxidation of CO is considered. The CO species adsorbed on the pristine surface is able to uptake an oxygen atom from a bridge site, generating CO_2, and the process is 0.28 eV endothermic, which is 0.31 eV less than the same process at the V/C interface. Therefore, CO could be spontaneously converted to CO_2 in the presence of the solvent at certain temperatures and reduce the surface sites at the same time.

CO binds more strongly to the O_v site than to the pristine surface at the S/C interface. Since the CO reduction reaction is supposed to follow the single electron transfer rule, where only one proton and one electron participate in each step, the CO species would convert to the CH_3OH and CH_4 products through the CHO*, CH_2O*, CH_3O* or CH_2OH* intermediates, based on our previous investigation (see Figures 4a and S4). At the V/C interface (black line in Figure 4), the adsorbed CO successively binds protons at the carbon site in the first two hydrogenation steps, with enthalpy variations of 0.06 eV and -0.81 eV, respectively. The first step producing the CH_2O* intermediate has a larger activation energy of 1.41 eV. The CH_2O* intermediate binds to the surface strongly, which has to combine with another proton at the carbon site with a barrier of 0.80 eV, to generate the CH_3O* intermediate, and releasing a considerable amount of energy (1.27 eV). There is an alternative feasible pathway where the oxygen site of the CH_2O* intermediate binds a proton to generate CH_2OH*, with a barrier higher by 0.19 eV, and reaction endothermicity of 0.33 eV. The presence of the solvent does not create a big difference in the reaction profile (the red and the black pathways in Figure 4 nearly overlap). In fact, the maximum cumulative difference of these steps is only 0.08 eV.

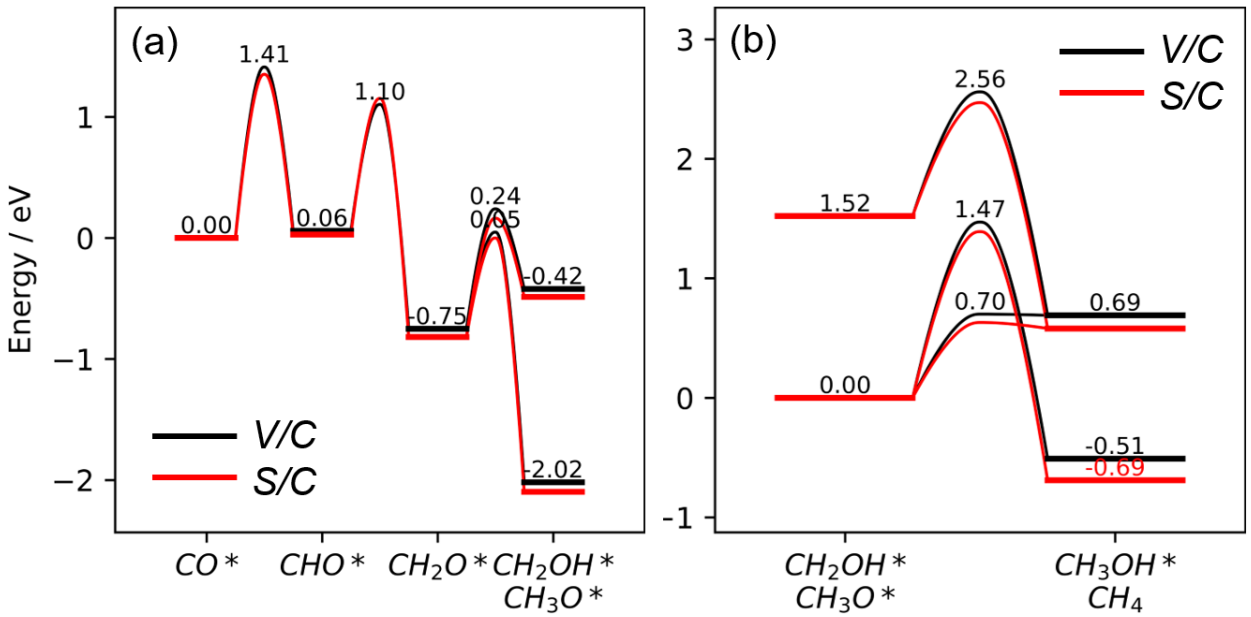

Figure 4. The calculated reaction profile of CO* conversion: (a) from CO to CH_3O*/CH_2OH*, and (b) from CH_3O*/CH_2OH* to CH_4/CH_3OH. All corresponding configurations are displayed in Figure S5.

Both CH_3O* and CH_2OH* intermediates can participate in the final hydrogenation step to generate the products, CH_3OH and CH_4, as illustrated in Figure 4 and S4. During the final hydrogenation process at the V/C interface, the CH_3O* intermediate preferentially exothermically binds with a proton at the carbon site, heals O_v with its oxygen atom and generates methane. The barrier for this step is as high as 1.47 eV, making it the rate-determining step. CH_3O* also can bind a proton at the oxygen site, forming the CH_3OH* intermediate, with a 0.77 eV lower barrier. However, the reaction energy for this alternative process is 0.69 eV, and the desorption energy for methanol is 1.21 eV, which makes the process thermodynamically forbidden. Similarly, in spite of an exothermic production of CH_3OH*, with a lower activation energy of 1.04 eV, the CH_2OH* intermediate finally results in CH_4, because of the strong adsorption of methanol. Thus, only methane is generated at the V/C interface of the defective surface. When this process happens at the S/C interface, the solvent effect slightly enhances the reactions. The enthalpies of all reaction steps decrease by more than 0.1 eV, and the corresponding barriers also have obvious downshifts. Because of the weak adsorption of methanol at the S/C interface, the pathway involving the CH_2OH* intermediate is the kinetically favorable to generate methanol.

Overall, at the V/C interface, because of the strong adsorption of methanol, CH_4 is produced from CO_2 through the $CO_2 \rightarrow CO^* \rightarrow CHO^* \rightarrow CH_2O^* \rightarrow CH_3O^* \rightarrow CH_4$ pathway (i.e. the CH_3O* pathway). On the other hand, at the S/C interface, methanol could be a feasible and kinetically preferred product, produced via $CO^* \rightarrow CHO^* \rightarrow CH_2O^* \rightarrow CH_2OH^* \rightarrow CH_3OH^* \rightarrow CH_3OH$ (i.e. the CH_3OH pathway). To summarize, a scheme of the reactions occurring at the S/C interface is shown in Figure 5, which surprisingly suggests that CO as the most feasible reactant in this reaction, and CO_2, CH_3OH and CH_4 are the products. However, the main product in these conditions is still the methane, since the barriers of producing methane and hydrogenating CO similar. If there is plenty formaldehyde yielded by the pristine surface participating in this pathway, the main product should be the methanol. This is consistent with the experiments showing that the product for CO_2 reduction reaction on anatase TiO_2 is CO and CH_4 in the gas/solid reaction[49–52], but CO, CH_4, and CH_3OH could

be generated at the liquid/solid interface[53,54]. Beyond that, we find that the solvent effect greatly impacts the beginning and ending of a pathway (adsorption and desorption process), but influences the intermediate steps only slightly.

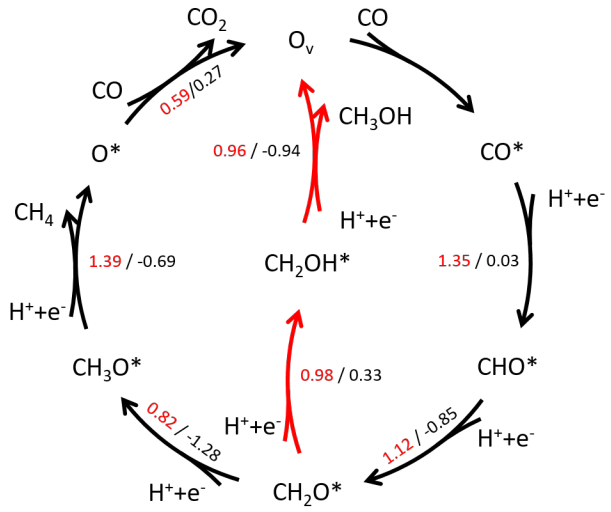

Figure 5. The schematic diagram of CO_2 (CO) reduction catalytic cycle at the S/C interface on the defective anatase surface. The black arrows illustrate the thermodynamically favorable pathway, and the red arrows show the kinetic favorable pathway. The red and black numbers represent for the activation energy and the enthalpy variation of the corresponding reaction steps, respectively.

The adsorption and reaction processes at the electrolyte/catalyst (E/C) interface of the defective surface

The adsorption energies of all involved reactants and products calculated as a function of ϕ_{SHE} are shown in Figure 6. Since the variation of ϕ_{SHE} is depended on the applied negative bias, the way we describe the profiles is along the direction of decreasing ϕ_{SHE} in the following works. In order to explore the stability of TiO_2 under negative (i.e., reducing) potentials, we ran experimental measurements (see Supporting Information) using an amorphous TiO_2 catalyst deposited by atomic layer deposition (ALD)[24,26,27,55] over the course of a 10 h reaction. The stability of the simulated system was tested by depositing 5nm thick layer of TiO_2 on ITO substrates using ALD. CO_2 reduction was performed in a three terminal potentiostat for 10 hours in the 0.5mol KCl with pH=7 buffer solution while continuously bubbling CO_2 through the solution with the working electrode held at -0.6 V vs NHE. Current vs potential measurements were taken before and after the 10 hours reaction, as plotted in Figure S6. Here, we see an increase in the electrochemical current during the course of the measurement indicating an increase in the O-vacancy concentration due to the applied reducing potentials. X-ray photoemission spectra (XPS) taken before and after the 10 hours reaction provide further evidence for the increase in O-vacancy density. These spectra show an increase in the non-stoichiometric Ti^{3+} states (which correspond to O-vacancies) from 0.031 to 0.048, as indicated in the Figure S7. We believe that the increase in Ti^{3+} states is due to the growth of O-vacancies rather than the build-up of the Ti_2O_3 phase, since it is difficult to convert TiO_2 to Ti_2O_3 electrochemically. The transformation between these two phases entails a very high energy barrier, which requires annealing to overcome[56]. Depending on Figure 6a, the CO_2 still cannot exothermically bind to either surface, suggesting the dissolved CO_2 has to be converted before taking part in the

reaction. The CO, on the other hand, has the capacity of adsorbed on the pristine surface with a rather large range of ϕ_{SHE}. It is also exothermically adsorbed at the O_v site below the ϕ_{SHE} of -0.28 V. Therefore, the reactive window is defined from -0.6 ~ -0.28 V, where the upper limit depends on the adsorption of the CO species and the lower limit is on the limitation of the experiment. In terms of the products (Figure 6b), all of them would directly or indirectly desorb from the surface except for the CH_2O species which has a considerable adsorption energy on the defective surface at certain ϕ_{SHE}.

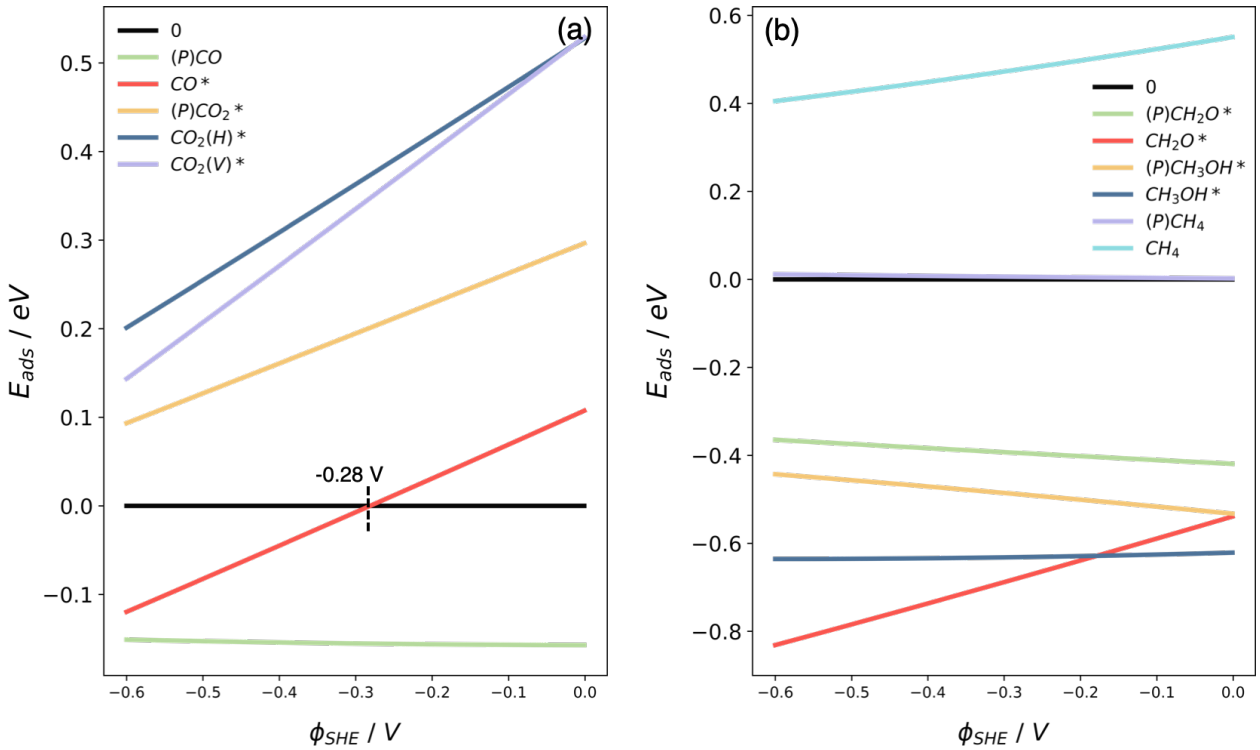

Figure 6. The calculated adsorption energies as a function of applied electrochemical potential. The black solid line is the benchmark of 0 eV.

It is noteworthy that some binding energies exhibit uptrends, and others exhibit downtrends as a function of ϕ_{SHE}. In order to elucidate the underlying reason, the charge transfer upon the molecular chemical adsorption at the S/C interface was studied (Table 2), where the positive values indicate the corresponding adsorbed molecules are oxidants, while the negative values refer to reductants. Within this definition, carbon oxides are oxidants at both surface sites, and, interestingly, the CH_2O at the defective surface is also an oxidant. From Figure 6, it is quite clear that all binding energies of adsorbed oxidants have a same trend that becoming more stable with an increasing bias, *vice versa* for the reductants. We think the charge transfer plays an important role in this process. As shown before, the introduced excess charge mainly accumulates at and near the surface of the electrode, which thus becomes more reducing, upon increasing net charge and decreasing ϕ_{SHE}. Therefore, the bound oxidants can withdraw more electrons and become more stable. On the other hand, the surface-bound reductants cannot readily donate electrons to the surface and destabilize accordingly. Here, the diffusion process, *i.e.* adsorption and desorption of reactants and products, which is supposed controlled by ϕ_{SHE}, could affect the reaction process. Hence, we think the diffusion process is one factor to determine the onset potential.

Table 2 The charge transfer of chemical adsorbed molecules at the S/C interface of both pristine and defective surface.

	Charge transfer from the surface slab / e	
Adsorbates	Pristine surface	Defective surface
CO_2	0.28	1.88
CO	--	0.67
CH_2O	-0.16	1.55
CH_3OH	-0.19	-0.2

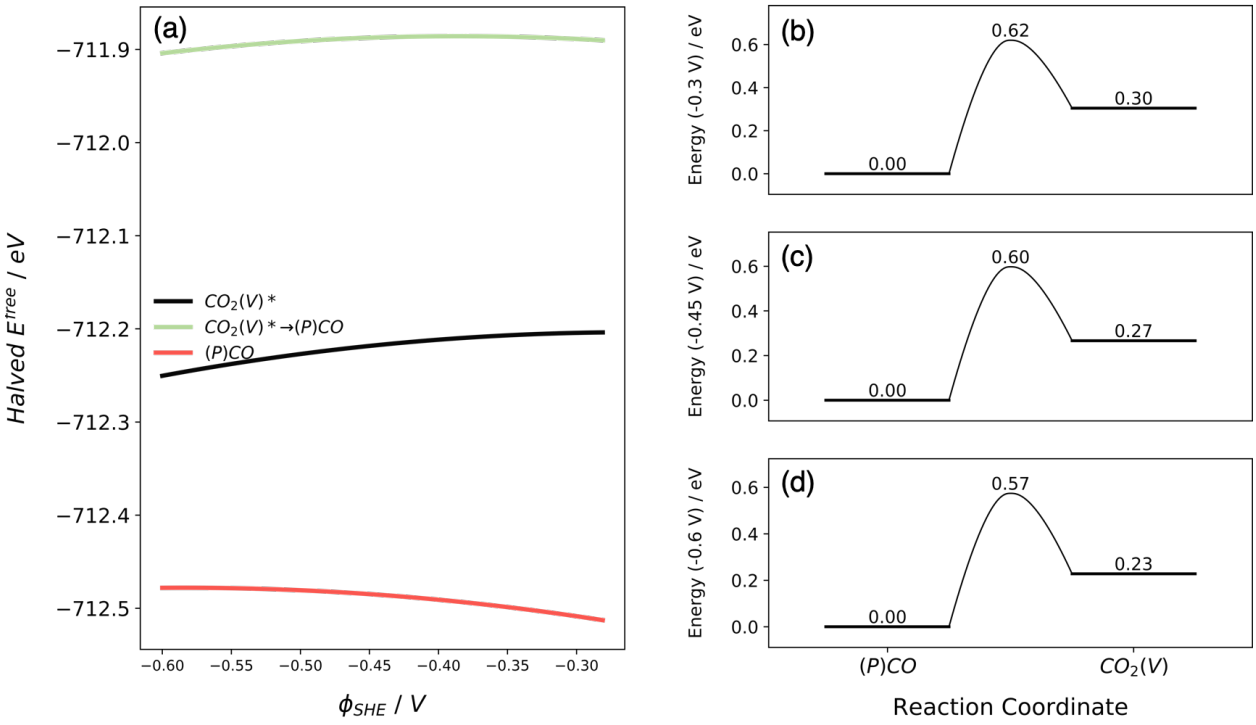

Figure 7. The electronic free energies as a function of applied electrochemical potential (a) on the conversion between the carbon oxides and the corresponding snapshots at the ϕ_{SHE} of -0.3 V (b), -0.45 V (c) and -0.6 V (d).

The conversion between CO and CO_2 at the E/C interface of the pristine surface was calculated (Figure 7). In the existence of the ϕ_{SHE}, the CO oxidation process becomes a little harder in the beginning (-0.3 V) and slightly better (-0.6 V) with the increasing negative bias. Under this condition, the CO species still reduces the surface as its performance at the S/C interface.

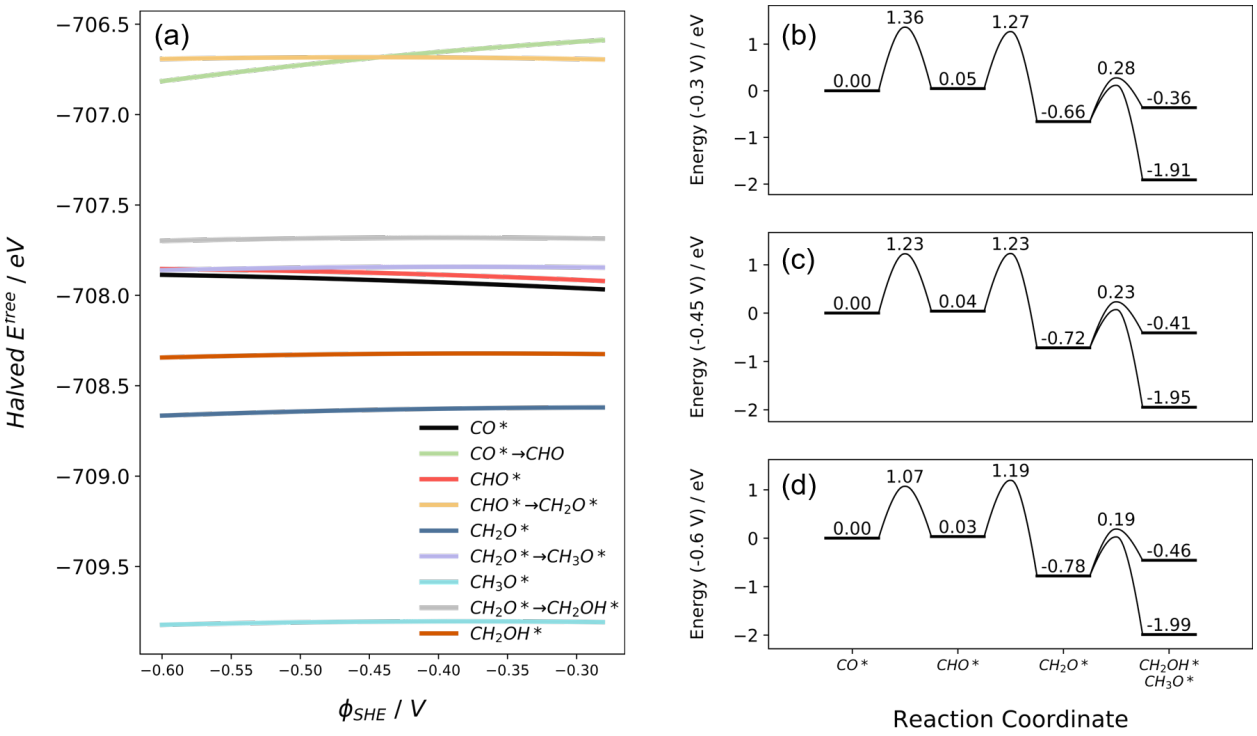

Figure 8. The electronic free energies as a function of applied electrochemical potential (a) on the conversion of the CO species and the corresponding snapshots at the ϕ_{SHE} of -0.3 V (b), -0.45 V (c) and -0.6 V (d).

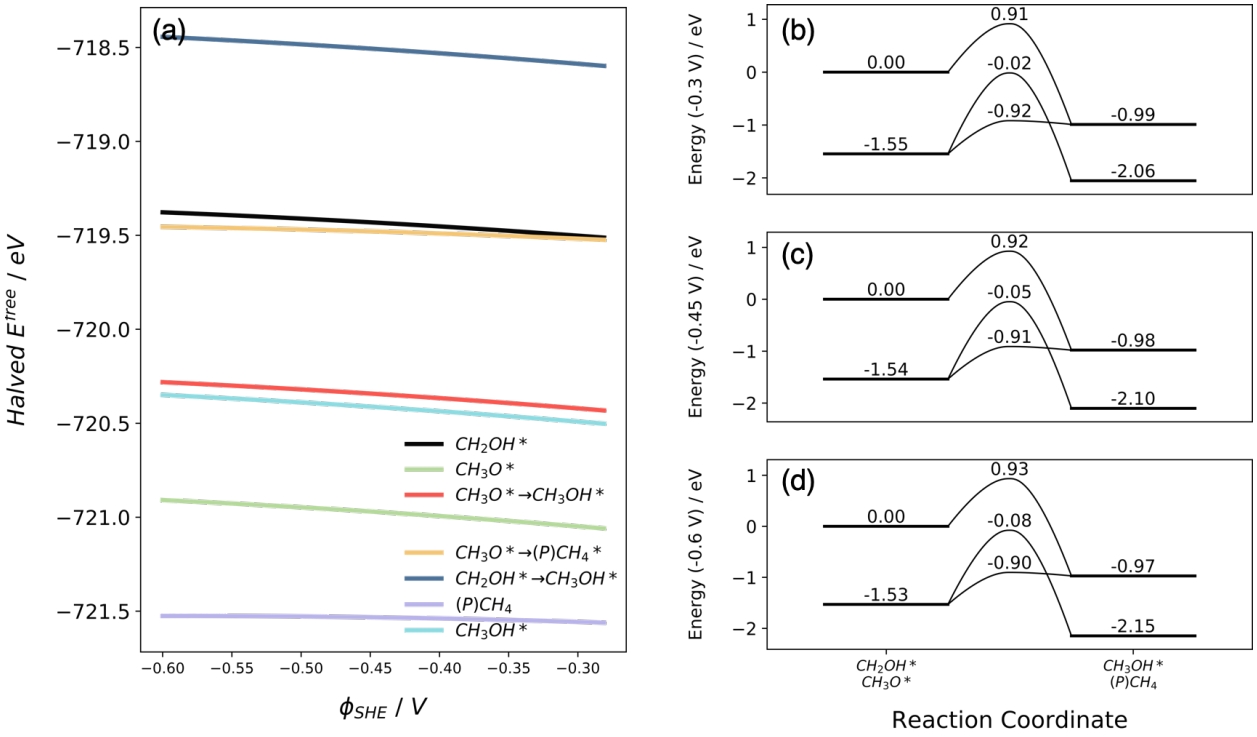

Figure 9. The electronic free energies as a function of applied electrochemical potential (a) on the product generation steps and the corresponding snapshots at the ϕ_{SHE} of -0.3 V (b), -0.45 V (c) and -0.6 V (d).

The hydrogenation reactions of CO at the O_v site are studied at the E/C interface below the ϕ_{SHE} of -0.28 V (Figure 8, 9). For the S/C interface, there were two pathways: a kinetically favorable one that yields CH_3OH, and the other one forming CH_4. The main product should be the methane because of the similar barriers of hydrogenating CO and generating CH_4. In the presence of ϕ_{SHE}, the barrier of the CO hydrogenation has a dramatical drop along the potential (Figure 8a), while the CH_4 generation one remains at a certain level (Figure 9a). At the ϕ_{SHE} of -0.3 V, for instance, the activation energy of first hydrogenation step reduces to 1.36 eV (Figure 8b), whereas the $CH_3O^* \rightarrow CH_4$ one grows to 1.53 eV (Figure 9b) compared with the S/C interface. Therefore, the kinetically favorable pathway, *i.e.* the CH_3OH pathway, becomes the main process at the E/C interface with an appropriate temperature. The rate-determined step is the first hydrogenation one with the activation energy of 1.36 eV at -0.3 V. As the negative bias increases, all involved enthalpy variations and activation energies have different changes. At the ϕ_{SHE} of -0.45 V, barriers of the first, second and CH_3O^* hydrogenation steps decrease to different degrees (Figure 8c, 9c). Apart from the activation energies, the formation energies change as well and the CH_2O intermediate become more stable, for instance. When the ϕ_{SHE} reaches -0.6 V, the barrier of the second hydrogenation step reduces to 1.16 eV (Figure 8d), which is close to the increasing barrier of the CH_3OH generation step (0.93 eV, Figure 9d). Overall, in the presence of a lower applied negative bias, the final product favors in the methanol instead, which is consistent with the experiment[26,28].

The deoxygenation pathway of methane generation at the defective surface

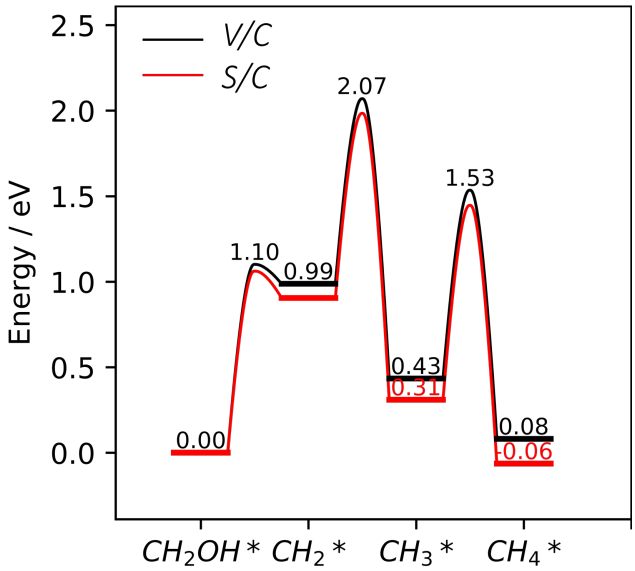

Figure 10. The reaction profile of a possible deoxygenation pathway of CH_2OH^* at the V/C and S/C interfaces of the defective surface. All corresponding configurations are displayed in Figure S8.

Even though the CH_3O^* pathway in the last section is not competitive with the CH_3OH one at the E/C interface, the experiment still found methane being produced[57]. One possible reason is that methane could be generated at the pristine surface. Alternatively, a deoxygenation pathway involving the removal of oxygen before the initial hydrogenation step, proposed by Ji et al., could be envisioned. However, this pathway has been proven

impossible at both the pristine and the defective surfaces[58,59]. It is also conceivable that oxygen would dissociate away as a hydroxyl group, rather than O (curing the O_v), for fulfilling a catalytic cycle. In our previous work on anatase without solvent or electrochemical potential, the deoxygenation step of the CHOH* intermediate was 1.74 eV uphill, and had an activation energy of 1.96 eV, *i.e.* less favorable than the original CH_3O* pathway. In this study, a dissociation step of the CH_2OH* intermediate was calculated at the S/C interface of the defective surface (Figure 10). The reaction energy of the deoxygenation step decreased to 0.99 eV at the V/C interface of the defective surface, and the corresponding barrier is only 1.10 eV, which is lower than the rate-determined barrier of the CH_3O* path. The products of this step are the CH_2* intermediate and an OH radical. The OH radical is likely to accept an electron from the cathode and migrate to the counter electrode, and the CH_2* intermediate becomes available to participate in the following reaction steps. The hydrogenation steps afterwards are downhill, with the similar barriers as the deoxygenation step, and result in CH_4. In the presence of the solvent, both the activation and the reaction energies of these subsequent steps are slightly lowered (by ca. 0.1 eV), with the exception of the final step, which experiences a 0.04 eV increase in the activation energy. Even though the reaction energy of the deoxygenation step nearly halved, the remainder of the pathway is still too energy-demanding to compete with the CH_3O* pathway at the S/C interface at the room temperature.

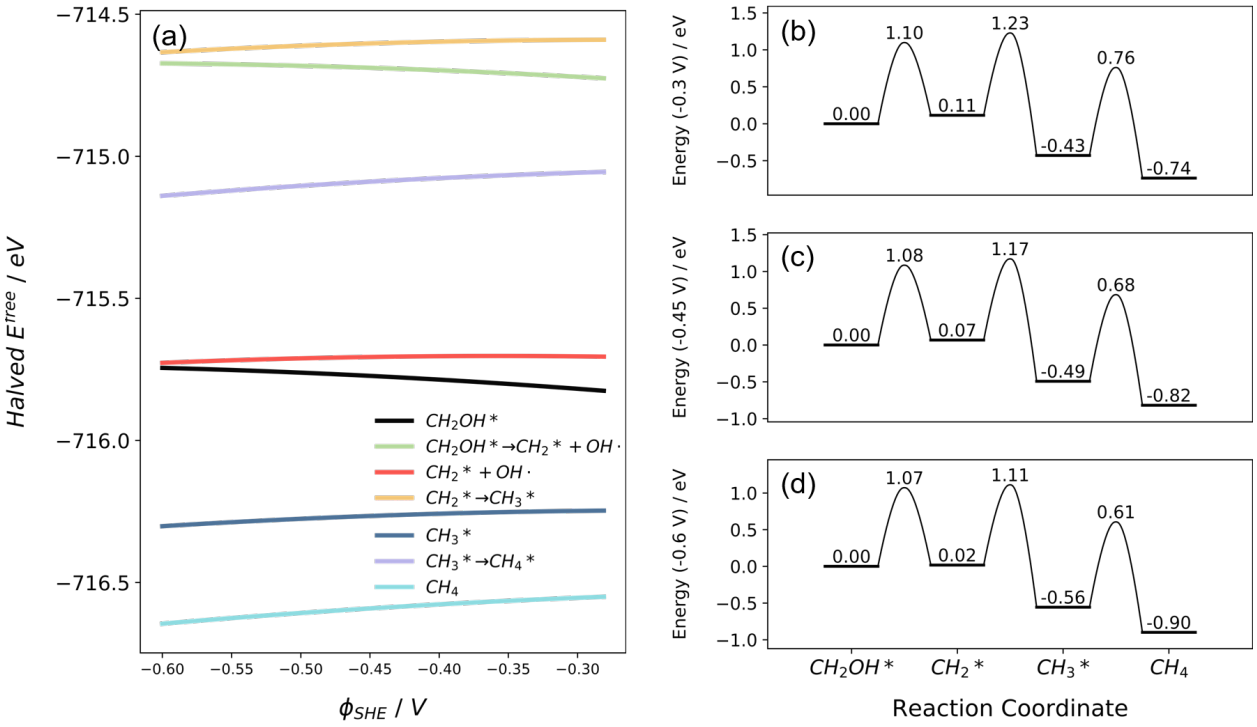

Figure 11. The electronic free energies as functions of applied electrochemical potential (a) on the deoxygenation pathway and the corresponding snapshots at the ϕ_{SHE} of -0.3 V (b), -0.45 V (c) and -0.6 V (d).

However, this deoxygenation step is heavily depended on the ϕ_{SHE} according to our calculation on the deoxygenation pathway at the E/C interface of the defective surface (Figure 11). At the ϕ_{SHE} of -0.3 V (Figure 11b), the corresponding enthalpy variation drops by 0.81 eV compared with the S/C interface to make the deoxygenation pathways feasible at room temperature. Meanwhile, the applied bias also exerts a slight negative

influence on all involved activation energies. As the bias increases, all influenced barriers suffer a downtrend (Figure 11d), which approach the barrier of CH_3OH generation step. However, at -0.6 V, the rate-determined step of the deoxygenation pathway is still higher than that of the CH_3OH one, which makes the latter the dominated pathway.

In conclusion, the catalytic cycle in the presence of ϕ_{SHE} is such that the adsorbed CO mainly follows the CH_3OH pathway that has a rate-determined barrier of 1.16 eV and generates methanol at -0.6 V as illustrated in Figure 12. Compared with the CH_3OH and deoxygenation pathways at the S/C interface, the pathways are dramatically improved by the applied bias. If there is the formaldehyde species generated from the pristine surface, it would directly occupy the O_v site and produce methanol or methane along the pathways at the E/C interface of defective surface. Here, the reaction process is controlled by the potential depended thermodynamic and kinetic process, which are thought to be another factor to determine the onset potential.

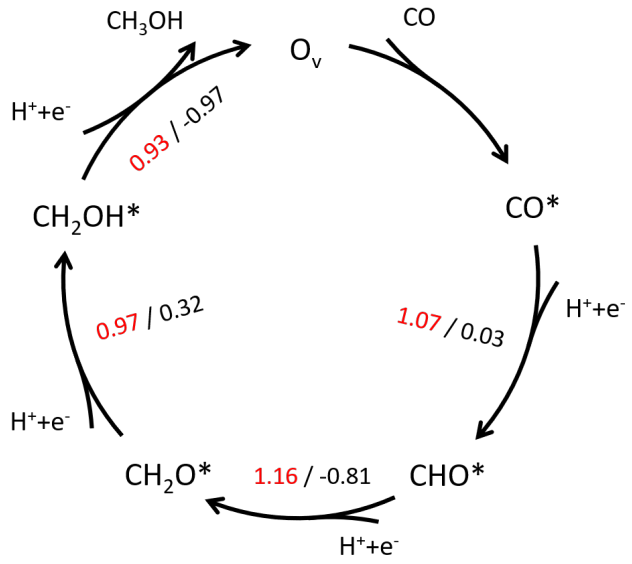

Figure 12. The schematic diagram of CO_2 reduction reaction catalytic cycle at the E/C interface of defective surface with a ϕ_{SHE} of -0.6 V. The red and black numbers represent for the activation energy and the enthalpy variation of corresponding reaction steps, respectively.

Conclusions

The adsorption and reaction mechanisms involved in the CO_2 reduction at both the solvent/catalyst and electrolyte/catalyst interfaces of the defective anatase TiO_2 (101) surface were investigated by DFT. We analyzed the charge distribution at the pristine and defective surface slabs, which are deeply influenced by the solvent and electrochemical potential. We reported the effect of the charge redistributions within the slab on the electronic structures and stabilities of the adsorbed species involved in the reaction in various conditions. We proposed two different the catalytic cycles operating at the S/C and the E/C interfaces.

While making a surface cut creates a great onset of ionic bonding character in the surface, the solvent effect is shown to electronically passivate it due to polarization interactions. As a result, the adsorption energies of all

involved molecules are weakened in the solvent, as compared to dry interface. That benefits desorption of products such as methanol, but deters the binding of the reactants such as the carbon oxides. When the surface slab is charged as a cathode, and the solvent becomes an electrolyte, the extra charge concentrates in the surface area, consistently with the behavior of a semiconductor electrode. This redistribution enhances the reducing ability of Ti and reduces the oxidizing ability of O at the surface. The binding of involved chemical species then further affected at the cathode, based on their redox properties.

The reaction mechanism at the S/C and E/C interfaces of defective surface is found to vary with the change of the reaction conditions. At the S/C interface, CO_2 cannot directly adsorb, and instead, produced CO tends to uptake an O atom from the surface, creating O_v and producing more CO_2. CO can also bind to the oxygen vacancy, and undergo photocatalytic hydrogenation, yielding CH_4 and CH_3OH, of which the latter is considered not to desorb at the V/C interface. Interestingly, the CO species is suggested by the calculation to be the main reactant at the S/C interface, forming CO_2, CH_4, and CH_3OH. The solvent effect is found to affect the reaction process only slightly, but greatly impact the adsorption/desorption process.

The mechanisms are also calculated controlled by diffusion and reaction processes, which are as a function of the applied electrochemical potential at the E/C interface. In the presence with bias, the conversion of CO to CH_3OH as the main products is kinetically favored. The adsorption of the main reactant, CO, is adsorbed under the potential below -0.28 V. Therefore, the onset potential involved in the (photo)electrochemical process are supposed to be controlled by both the diffusion and reaction processes.

Acknowledgments:

Financial support for the theory work comes from the CSC Fellowship to J.L. and the DOE-BES Award DE-SC0019152 to A.N.A.. We also acknowledge the UCLA-IDRE cluster Hoffman2 and XSEDE for computational resources. The experiment at USC was supported by the Air Force Office of Scientific Research (AFOSR) grant no. FA9550-19-1-0115 (R.L.) and the Army Research Office (ARO) award no. W911NF-17-1-0325 (H.S.).

Reference:

(1) Carbon Dioxide | Vital Signs – Climate Change: Vital Signs of the Planet https://climate.nasa.gov/vital-signs/carbon-dioxide/ (accessed Jun 4, 2019).

(2) Dhakshinamoorthy, A.; Navalon, S.; Corma, A.; Garcia, H. Photocatalytic CO2 Reduction by TiO2 and Related Titanium Containing Solids. *Energy Environ. Sci.* **2012**, *5* (11), 9217. https://doi.org/10.1039/c2ee21948d.

(3) Habisreutinger, S. N.; Schmidt-Mende, L.; Stolarczyk, J. K. Photocatalytic Reduction of CO_2 on TiO_2 and Other Semiconductors. *Angew. Chem. Int. Ed.* **2013**, *52* (29), 7372–7408. https://doi.org/10.1002/anie.201207199.

(4) Wu, J.; Huang, Y.; Ye, W.; Li, Y. CO_2 Reduction: From the Electrochemical to Photochemical Approach. *Adv. Sci.* **2017**, *4* (11), 1700194. https://doi.org/10.1002/advs.201700194.

(5) Xiong, Z.; Lei, Z.; Li, Y.; Dong, L.; Zhao, Y.; Zhang, J. A Review on Modification of Facet-Engineered TiO2 for Photocatalytic CO2 Reduction. *J. Photochem. Photobiol. C Photochem. Rev.* **2018**, *36*, 24–47.

https://doi.org/10.1016/j.jphotochemrev.2018.07.002.

(6) Dincer, I.; Acar, C. Review and Evaluation of Hydrogen Production Methods for Better Sustainability. *Int. J. Hydrog. Energy* **2015**, *40* (34), 11094–11111. https://doi.org/10.1016/j.ijhydene.2014.12.035.

(7) Xie, S.; Zhang, Q.; Liu, G.; Wang, Y. Photocatalytic and Photoelectrocatalytic Reduction of CO2 Using Heterogeneous Catalysts with Controlled Nanostructures. *Chem. Commun.* **2015**, *52* (1), 35–59. https://doi.org/10.1039/C5CC07613G.

(8) Halmann, M. Photoelectrochemical Reduction of Aqueous Carbon Dioxide on P-Type Gallium Phosphide in Liquid Junction Solar Cells. *Nature* **1978**, *275* (5676), 115–116. https://doi.org/10.1038/275115a0.

(9) Barton, E. E.; Rampulla, D. M.; Bocarsly, A. B. Selective Solar-Driven Reduction of CO_2 to Methanol Using a Catalyzed p-GaP Based Photoelectrochemical Cell. *J. Am. Chem. Soc.* **2008**, *130* (20), 6342–6344. https://doi.org/10.1021/ja0776327.

(10) Qiu, J.; Zeng, G.; Ha, M.-A.; Ge, M.; Lin, Y.; Hettick, M.; Hou, B.; Alexandrova, A. N.; Javey, A.; Cronin, S. B. Artificial Photosynthesis on TiO_2 -Passivated InP Nanopillars. *Nano Lett.* **2015**, *15* (9), 6177–6181. https://doi.org/10.1021/acs.nanolett.5b02511.

(11) Song, J. T.; Ryoo, H.; Cho, M.; Kim, J.; Kim, J.-G.; Chung, S.-Y.; Oh, J. Nanoporous Au Thin Films on Si Photoelectrodes for Selective and Efficient Photoelectrochemical CO_2 Reduction. *Adv. Energy Mater.* **2017**, *7* (3), 1601103. https://doi.org/10.1002/aenm.201601103.

(12) Tian, Z.; Priest, C.; Chen, L. Recent Progress in the Theoretical Investigation of Electrocatalytic Reduction of CO_2. *Adv. Theory Simul.* **2018**, *1* (5), 1800004. https://doi.org/10.1002/adts.201800004.

(13) Che, F.; Gray, J. T.; Ha, S.; Kruse, N.; Scott, S. L.; McEwen, J.-S. Elucidating the Roles of Electric Fields in Catalysis: A Perspective. *ACS Catal.* **2018**, *8* (6), 5153–5174. https://doi.org/10.1021/acscatal.7b02899.

(14) Lazzeri, M.; Vittadini, A.; Selloni, A. Structure and Energetics of Stoichiometric TiO_2 Anatase Surfaces. *Phys. Rev. B* **2001**, *63* (15), 155409. https://doi.org/10.1103/PhysRevB.63.155409.

(15) Filhol, J.-S.; Neurock, M. Elucidation of the Electrochemical Activation of Water over Pd by First Principles. *Angew. Chem. Int. Ed.* **2006**, *45*. https://doi.org/10.1002/anie.200502540.

(16) Steinmann, S. N.; Michel, C.; Schwiedernoch, R.; Sautet, P. Impacts of Electrode Potentials and Solvents on the Electroreduction of CO_2: A Comparison of Theoretical Approaches. *Phys. Chem. Chem. Phys.* **2015**, *17* (21), 13949–13963. https://doi.org/10.1039/C5CP00946D.

(17) Kang, J.; Wei, S.-H.; Zhu, K.; Kim, Y.-H. First-Principles Theory of Electrochemical Capacitance of Nanostructured Materials: Dipole-Assisted Subsurface Intercalation of Lithium in Pseudocapacitive TiO_2 Anatase Nanosheets. *J. Phys. Chem. C* **2011**, *115* (11), 4909–4915. https://doi.org/10.1021/jp1090125.

(18) Lespes, N.; Filhol, J.-S. Using Implicit Solvent in Ab Initio Electrochemical Modeling: Investigating Li+/Li Electrochemistry at a Li/Solvent Interface. *J. Chem. Theory Comput.* **2015**, *11* (7), 3375–3382. https://doi.org/10.1021/acs.jctc.5b00170.

(19) Huang, Y.; Nielsen, R. J.; Goddard, W. A. Reaction Mechanism for the Hydrogen Evolution Reaction on the Basal Plane Sulfur Vacancy Site of MoS_2 Using Grand Canonical Potential Kinetics. *J. Am. Chem. Soc.* **2018**, *140* (48), 16773–16782. https://doi.org/10.1021/jacs.8b10016.

(20) Nørskov, J. K.; Rossmeisl, J.; Logadottir, A.; Lindqvist, L.; Kitchin, J. R.; Bligaard, T.; Jónsson, H. Origin of the Overpotential for Oxygen Reduction at a Fuel-Cell Cathode. *J. Phys. Chem. B* **2004**, *108* (46), 17886–17892. https://doi.org/10.1021/jp047349j.

(21) Roldan, A. Frontiers in First Principles Modelling of Electrochemical Simulations. *Curr. Opin. Electrochem.* **2018**, *10*, 1–6. https://doi.org/10.1016/j.coelec.2018.03.013.

(22) Aarik, J.; Aidla, A.; Uustare, T.; Sammelselg, V. Morphology and Structure of TiO2 Thin Films Grown by Atomic Layer Deposition. *J. Cryst. Growth* **1995**, *148* (3), 268–275. https://doi.org/10.1016/0022-0248(94)00874-4.

(23) Natarajan, C.; Fukunaga, N.; Nogami, G. Titanium Dioxide Thin Film Deposited by Spray Pyrolysis of Aqueous Solution. *Thin Solid Films* **1998**, *322* (1–2), 6–8. https://doi.org/10.1016/S0040-6090(97)01010-9.

(24) Chen, Y. W.; Prange, J. D.; Dühnen, S.; Park, Y.; Gunji, M.; Chidsey, C. E. D.; McIntyre, P. C. Atomic Layer-Deposited Tunnel Oxide Stabilizes Silicon Photoanodes for Water Oxidation. *Nat. Mater.* **2011**, *10* (7), 539–544. https://doi.org/10.1038/nmat3047.

(25) Lee, M. H.; Takei, K.; Zhang, J.; Kapadia, R.; Zheng, M.; Chen, Y.-Z.; Nah, J.; Matthews, T. S.; Chueh, Y.-L.; Ager, J. W.; et al. P-Type InP Nanopillar Photocathodes for Efficient Solar-Driven Hydrogen Production. *Angew. Chem. Int. Ed.* **2012**, *51* (43), 10760–10764. https://doi.org/10.1002/anie.201203174.

(26) Zeng, G.; Qiu, J.; Li, Z.; Pavaskar, P.; Cronin, S. B. CO_2 Reduction to Methanol on TiO_2 -Passivated GaP Photocatalysts. *ACS Catal.* **2014**, *4* (10), 3512–3516. https://doi.org/10.1021/cs500697w.

(27) Hu, S.; Shaner, M. R.; Beardslee, J. A.; Lichterman, M.; Brunschwig, B. S.; Lewis, N. S. Amorphous TiO2 Coatings Stabilize Si, GaAs, and GaP Photoanodes for Efficient Water Oxidation. *Science* **2014**, *344* (6187), 1005–1009. https://doi.org/10.1126/science.1251428.

(28) Szaniawska, E.; Bienkowski, K.; Rutkowska, I. A.; Kulesza, P. J.; Solarska, R. Enhanced Photoelectrochemical CO2-Reduction System Based on Mixed Cu2O – Nonstoichiometric TiO2 Photocathode. *Catal. Today* **2018**, *300*, 145–151. https://doi.org/10.1016/j.cattod.2017.05.099.

(29) Liu, J.-Y.; Gong, X.-Q.; Alexandrova, A. N. Mechanism of CO_2 Photocatalytic Reduction to Methane and Methanol on Defected Anatase TiO_2 (101): A Density Functional Theory Study. *J. Phys. Chem. C* **2019**, *123* (6), 3505–3511. https://doi.org/10.1021/acs.jpcc.8b09539.

(30) Kresse, G.; Hafner, J. Ab Initio Molecular Dynamics for Liquid Metals. *Phys. Rev. B* **1993**, *47* (1), 558–561. https://doi.org/10.1103/PhysRevB.47.558.

(31) Kresse, G.; Hafner, J. Ab Initio Molecular-Dynamics Simulation of the Liquid-Metal–Amorphous-Semiconductor Transition in Germanium. *Phys. Rev. B* **1994**, *49* (20), 14251–14269. https://doi.org/10.1103/PhysRevB.49.14251.

(32) Kresse, G.; Furthmüller, J. Efficiency of Ab-Initio Total Energy Calculations for Metals and Semiconductors Using a Plane-Wave Basis Set. *Comput. Mater. Sci.* **1996**, *6* (1), 15–50. https://doi.org/10.1016/0927-0256(96)00008-0.

(33) Kresse, G.; Furthmüller, J. Efficient Iterative Schemes for Ab Initio Total-Energy Calculations Using a Plane-Wave Basis Set. *Phys. Rev. B* **1996**, *54* (16), 11169–11186. https://doi.org/10.1103/PhysRevB.54.11169.

(34) Blöchl, P. E. Projector Augmented-Wave Method. *Phys. Rev. B* **1994**, *50* (24), 17953–17979. https://doi.org/10.1103/PhysRevB.50.17953.

(35) Kresse, G.; Joubert, D. From Ultrasoft Pseudopotentials to the Projector Augmented-Wave Method. *Phys. Rev. B* **1999**, *59* (3), 1758–1775. https://doi.org/10.1103/PhysRevB.59.1758.

(36) Perdew, J. P.; Burke, K.; Ernzerhof, M. Generalized Gradient Approximation Made Simple. *Phys. Rev.*

Lett. **1996**, *77* (18), 3865–3868. https://doi.org/10.1103/PhysRevLett.77.3865.

(37) Perdew, J. P.; Burke, K.; Ernzerhof, M. Generalized Gradient Approximation Made Simple [Phys. Rev. Lett. 77, 3865 (1996)]. *Phys. Rev. Lett.* **1997**, *78* (7), 1396–1396. https://doi.org/10.1103/PhysRevLett.78.1396.

(38) Mathew, K.; Sundararaman, R.; Letchworth-Weaver, K.; Arias, T. A.; Hennig, R. G. Implicit Solvation Model for Density-Functional Study of Nanocrystal Surfaces and Reaction Pathways. *J. Chem. Phys.* **2014**, *140* (8), 084106. https://doi.org/10.1063/1.4865107.

(39) Mathew, K.; Hennig, R. G. Implicit Self-Consistent Description of Electrolyte in Plane-Wave Density-Functional Theory. *ArXiv160103346 Cond-Mat* **2016**.

(40) Henkelman, G.; Uberuaga, B. P.; Jónsson, H. A Climbing Image Nudged Elastic Band Method for Finding Saddle Points and Minimum Energy Paths. *J. Chem. Phys.* **2000**, *113* (22), 9901–9904. https://doi.org/10.1063/1.1329672.

(41) Tang, W.; Sanville, E.; Henkelman, G. A Grid-Based Bader Analysis Algorithm without Lattice Bias. *J. Phys. Condens. Matter* **2009**, *21* (8), 084204. https://doi.org/10.1088/0953-8984/21/8/084204.

(42) Steinmann, S. N.; Sautet, P. Assessing a First-Principles Model of an Electrochemical Interface by Comparison with Experiment. *J. Phys. Chem. C* **2016**, *120* (10), 5619–5623. https://doi.org/10.1021/acs.jpcc.6b01938.

(43) Trasatti, S. The Absolute Electrode Potential: An Explanatory Note: (Recommendations 1986). https://doi.org/10.1515/iupac.58.0011.

(44) Taylor, C. D.; Wasileski, S. A.; Filhol, J.-S.; Neurock, M. First Principles Reaction Modeling of the Electrochemical Interface: Consideration and Calculation of a Tunable Surface Potential from Atomic and Electronic Structure. *Phys. Rev. B* **2006**, *73* (16). https://doi.org/10.1103/PhysRevB.73.165402.

(45) Panayotov, D. A.; Yates, J. T. N-Type Doping of TiO2 with Atomic Hydrogen-Observation of the Production of Conduction Band Electrons by Infrared Spectroscopy. *Chem. Phys. Lett.* **2007**, *436* (1), 204–208. https://doi.org/10.1016/j.cplett.2007.01.039.

(46) Islam, M. M.; Calatayud, M.; Pacchioni, G. Hydrogen Adsorption and Diffusion on the Anatase TiO2(101) Surface: A First-Principles Investigation. *J. Phys. Chem. C* **2011**, *115* (14), 6809–6814. https://doi.org/10.1021/jp200408v.

(47) Mosconi, E.; Selloni, A.; De Angelis, F. Solvent Effects on the Adsorption Geometry and Electronic Structure of Dye-Sensitized TiO $_2$: A First-Principles Investigation. *J. Phys. Chem. C* **2012**, *116* (9), 5932–5940. https://doi.org/10.1021/jp209420h.

(48) He, H.; Zapol, P.; Curtiss, L. A. A Theoretical Study of CO2 Anions on Anatase (101) Surface. *J. Phys. Chem. C* **2010**, *114* (49), 21474–21481.

(49) Anpo, M.; Yamashita, H.; Ichihashi, Y.; Ehara, S. Photocatalytic Reduction of CO2 with H2O on Various Titanium Oxide Catalysts. *J. Electroanal. Chem.* **1995**, *396* (1), 21–26. https://doi.org/10.1016/0022-0728(95)04141-A.

(50) Tan, S. S.; Zou, L.; Hu, E. Photocatalytic Reduction of Carbon Dioxide into Gaseous Hydrocarbon Using TiO2 Pellets. *Catal. Today* **2006**, *115* (1–4), 269–273. https://doi.org/10.1016/j.cattod.2006.02.057.

(51) Liu, L.; Zhao, H.; Andino, J. M.; Li, Y. Photocatalytic CO $_2$ Reduction with H $_2$ O on TiO $_2$ Nanocrystals: Comparison of Anatase, Rutile, and Brookite Polymorphs and Exploration of Surface Chemistry. *ACS Catal.* **2012**, *2* (8), 1817–1828. https://doi.org/10.1021/cs300273q.

(52) Yu, J.; Low, J.; Xiao, W.; Zhou, P.; Jaroniec, M. Enhanced Photocatalytic CO2-Reduction Activity of Anatase TiO2 by Coexposed {001} and {101} Facets. *J. Am. Chem. Soc.* **2014**, *136* (25), 8839–8842. https://doi.org/10.1021/ja5044787.

(53) Dey, G. R.; Pushpa, K. K. Formation of Different Products during Photo-Catalytic Reaction on TiO2 Suspension in Water with and without 2-Propanol under Diverse Ambient Conditions. *Res. Chem. Intermed.* **2007**, *33* (7), 631–644. https://doi.org/10.1163/156856707781749883.

(54) Kočí, K.; Obalová, L.; Matějová, L.; Plachá, D.; Lacný, Z.; Jirkovský, J.; Šolcová, O. Effect of TiO2 Particle Size on the Photocatalytic Reduction of CO2. *Appl. Catal. B Environ.* **2009**, *89* (3–4), 494–502. https://doi.org/10.1016/j.apcatb.2009.01.010.

(55) Qiu, J.; Zeng, G.; Ha, M.-A.; Hou, B.; Mecklenburg, M.; Shi, H.; Alexandrova, A. N.; Cronin, S. B. Microscopic Study of Atomic Layer Deposition of TiO_2 on GaAs and Its Photocatalytic Application. *Chem. Mater.* **2015**, *27* (23), 7977–7981. https://doi.org/10.1021/acs.chemmater.5b03246.

(56) Xu, M.; Zada, A.; Yan, R.; Li, H.; Sun, N.; Qu, Y. Ti_2O_3 /TiO_2 Heterophase Junctions with Enhanced Charge Separation and Spatially Separated Active Sites for Photocatalytic CO_2 Reduction. *Phys. Chem. Chem. Phys.* **2020**, 10.1039.C9CP05147C. https://doi.org/10.1039/C9CP05147C.

(57) Zhang, L.; Cao, H.; Pen, Q.; Wu, L.; Hou, G.; Tang, Y.; Zheng, G. Embedded CuO Nanoparticles@TiO2-Nanotube Arrays for Photoelectrocatalytic Reduction of CO2 to Methanol. *Electrochimica Acta* **2018**, *283*, 1507–1513. https://doi.org/10.1016/j.electacta.2018.07.072.

(58) Ip, C. M.; Troisi, A. A Computational Study of the Competing Reaction Mechanisms of the Photo-Catalytic Reduction of CO_2 on Anatase(101). *Phys Chem Chem Phys* **2016**, *18* (36), 25010–25021. https://doi.org/10.1039/C6CP02642G.

(59) Ji, Y.; Luo, Y. New Mechanism for Photocatalytic Reduction of CO_2 on the Anatase TiO_2 (101) Surface: The Essential Role of Oxygen Vacancy. *J. Am. Chem. Soc.* **2016**, *138* (49), 15896–15902. https://doi.org/10.1021/jacs.6b05695.

TOC Graphics: